ORIGINAL PAPER

A microscale three-dimensional urban energy balance model for studying surface temperatures

E. Scott Krayenhoff · James A. Voogt

Abstract A microscale three-dimensional (3-D) urban energy balance model, Temperatures of Urban Facets in 3-D (TUF-3D), is developed to predict urban surface temperatures for a variety of surface geometries and properties, weather conditions, and solar angles. The surface is composed of plane-parallel facets: roofs, walls, and streets, which are further sub-divided into identical square patches, resulting in a 3-D raster-type model geometry. The model code is structured into radiation, conduction and convection sub-models. The radiation sub-model uses the radiosity approach and accounts for multiple reflections and shading of direct solar radiation. Conduction is solved by finite differencing of the heat conduction equation, and convection is modelled by empirically relating patch heat transfer coefficients to the momentum forcing and the building morphology. The radiation and conduction sub-models are tested individually against measurements, and the complete model is tested against full-scale urban surface temperature and energy balance observations. Modelled surface temperatures perform well at both the facet-average and the sub-facet scales given the precision of the observations and the uncertainties in the model inputs. The model has several potential applications, such as the calculation of radiative loads, and the investigation of effective thermal anisotropy (when combined with a sensor-view model).

Keywords Microclimate · Model validation · Radiative exchange · Surface temperature · Thermal remote sensing · Urban energy balance model

E. S. Krayenhoff (✉)
Department of Geography, University of British Columbia, Vancouver, BC V6T 1Z2, Canada
e-mail: skrayenh@gmail.com

J. A. Voogt
Department of Geography, University of Western Ontario, London, ON N6A 5C2, Canada

List of Symbols

$c_{air,H}$	average heat capacity per unit plan area of air below z_H, $J\,m^{-2}\,K^{-1}$
C	volumetric heat capacities, $J\,m^{-3}\,K^{-1}$
e_a	water vapour pressure at z_{ref}, hPa
G	conductive heat flux density, $W\,m^{-2}$
H/W	mean building-height-to-street-width ratio of canyon or regular cube array
H/W_{3D}	mean wall-to-street area ratio of regular cube arrays
H_{can}	summed canopy patch convective sensible heat fluxes per canopy plan area, $W\,m^{-2}$
h	convective heat transfer coefficient (patch), $W\,m^{-2}\,K^{-1}$
H	convective sensible heat flux density (patch), $W\,m^{-2}$
h_{top}	convective heat transfer coefficient between canopy air and boundary layer, $W\,m^{-2}\,K^{-1}$
H_{top}	convective sensible heat flux density between canopy air and boundary layer, $W\,m^{-2}$
i, j	patch index/number
k	thermal conductivity, $W\,m^{-1}\,K^{-1}$
$K\!\uparrow$	upward shortwave radiative flux density, $W\,m^{-2}$
$K\!\downarrow_{dif}$	incident diffuse shortwave flux density, $W\,m^{-2}$
$K\!\downarrow_{dir}$	incident direct shortwave flux density, $W\,m^{-2}$
$K\!\downarrow_i$	incident shortwave radiative flux density at patch i after multiple reflections, $W\,m^{-2}$
$K\!\uparrow_i$	reflected shortwave radiative flux density at patch i after multiple reflections, $W\,m^{-2}$
L_h	forcing height for patch convection, m
l_p	length of a patch side, m
L_R	average roof length, m
$L\!\uparrow$	upward longwave radiative flux density, $W\,m^{-2}$
$L\!\downarrow$	downward longwave flux density from the sky, $W\,m^{-2}$
$L\!\downarrow_i$	incident longwave flux density at patch i after multiple reflections, $W\,m^{-2}$
m	timestep index
n	total number of patches
p	number of layers in a patch (conduction)
P_a	atmospheric pressure at z_{ref}, hPa
Q^*	net radiation flux density, $W\,m^{-2}$
Q_h	convective sensible heat flux density (volume), $W\,m^{-2}$
q	reflection number
R^q	reflected radiative flux density (solar or longwave) at reflection q, $W\,m^{-2}$
r_w	wall roughness coefficient
S_d	refers to the sub-domain
$T(z)$	air temperature at height z, K
T_a	air temperature at z_{ref}, K
T_{app}	apparent surface temperature, K

| $T_b \ (b = 1, \ldots, p)$	substrate layer temperatures, K
T_{can}	canopy air temperature ($z < z_H$), K
T_{D}	deep-soil temperature, K
T_{INT}	building internal temperature, K
$T_{\text{log}}(z)$	air temperature profile above z_H, K
T_R	mean roof surface temperature, K
T_r	mean road surface temperature, K
T_{sfc}	surface temperature, K
T_W	mean wall surface temperature, K
$U(z)$	wind speed at height z, m s^{-1}
U_{a}	wind speed at z_{ref}, m s^{-1}
$U_{\text{eff}}(z)$	effective wind speed at height z, m s^{-1}
x, y, z	location in space
x_L	building width, m
x_W	canyon (street) width, m
z_{0h}	roughness length for heat, m
z_{0m}	roughness length for momentum (patch), m
$z_{0\text{town}}$	roughness length for momentum (domain), m
z_{d}	displacement height, m
z_H	mean building height, m
z_{horz}	height of patch forcing $U(z)$ and $T(z)$ above street level, m
z_{ref}	reference height for forcing data, m
α	shortwave albedo
α_r	shortwave albedo of streets
α_R	shortwave albedo of roofs
α_W	shortwave albedo of walls
δ	solar azimuth angle, °
$\Delta\alpha_{\text{D}}$	sub-domain albedo change threshold
ΔQ_s	storage heat flux density (volume), W m^{-2}
Δt	timestep size, s
ΔT_{crit}	surface temperature change threshold, K
Δx	layer thickness, m
ε	longwave emissivity
ε_r	longwave emissivity of streets
ε_R	longwave emissivity of roofs
ε_W	longwave emissivity of walls
ϕ	solar zenith angle, °
γ	degree of implicitness (conduction)
η	domain rotation from north (clockwise), °
λ_c	complete-to-plan area ratio
λ_f	frontal-area-to-plan area ratio
λ_p	building-to-plan area ratio
λ_{pH}	building-to-plan area ratio at z_H
σ	Stefan–Boltzmann constant, W m^{-2} K^{-1}
Ω_{INT}	building internal resistance, W m^{-1} K^{-1}
$\psi_{i,\text{external}}$	view factor from a patch i to external surfaces
$\psi_{i,j}$	view factor from a patch i to a patch j
$\psi_{i,\text{sky}}$	view factor from a patch i to the sky

1 Introduction

The urban surface energy balance is essential to the understanding of urban climate and boundary-layer processes. Surface temperature is determined by the surface energy balance, and is related in a fundamental way to each of its component fluxes (with the exception of the solar forcing; Oke 1988). For example, each non-solar component flux can be mathematically expressed in terms of the surface temperature (Carlson et al. 1981). This is true for both urban and rural surfaces, but the former present a more varied and complex set of surface materials and geometries at local scales and microscales, rendering difficult generalizations about urban energy balances and surface temperature distributions.

This study investigates spatio-temporal distributions of urban surface temperatures down to the sub-facet scale (i.e. temperature distributions across walls, streets, and roofs). The observational record of these temperatures is mostly limited to scales of (or larger than) individual facets, and only for specific combinations of surface geometries and properties and weather conditions. Observations are labour- and cost-intensive to acquire at the sub-facet scale. Modelling has been slow to develop at these scales due to limits on computational power and a limited knowledge base with which to parameterise micrometeorological processes in complex urban environments, but a limited number of three-dimensional (3-D) building-resolving energy balance models currently exist (Terjung and Louie, 1974; Wu, 1995; Mills, 1997a; Bruse and Fleer, 1998; Ashie et al. 1999; Groleau et al. 2003; Kanda et al. 2005a). Here, development of the new Temperatures of Urban Facets in 3-D (TUF-3D) model, which accounts for the most important energy exchanges contributing to the distributions of urban surface temperature at sub-facet scales, is undertaken. Knowledge of surface temperature at sub-facet scales is important for a number of applications, including the design of buildings and neighbourhoods to maximise thermal efficiency (Mills 1997b), and the investigation of anisotropic thermal emission at the land-use scale (Voogt and Oke 1998).

TUF-3D simulates the energy balance over simple, non-vegetated, dry, plane-parallel 3-D urban surfaces on time scales of hours to days, resulting in surface temperature distributions down to the sub-facet scale. The goals of the work are to present the model theory and to demonstrate that TUF-3D performs adequately relative to available observations. A description of the model is given in Sect. 2, followed by tests of the radiation and conduction components, and finally by tests against full-scale observations.

2 Model design

TUF-3D represents the urban surface as a 3-D raster structure consisting of cells defined by the x and y (horizontal), and z (vertical) coordinates at their centres and 'containing' either building interior, ambient (e.g. canopy) air, or forming part of the base layer (at $z = 0$) of 1-cell thickness (Fig. 1). Buildings are most often represented as rectangular groups of cells of constant height; however, the model is constructed such that buildings may have any shape and spacing that conforms to the basic plane-parallel structure. When modelling regular arrays of buildings, an 'urban unit' defines the smallest plan area that encompasses all of the domain's morphological variation and repeats throughout the domain (Fig. 2). *Surface* patches with five possible orientations (downward-facing surfaces are excluded) are defined at the interfaces between
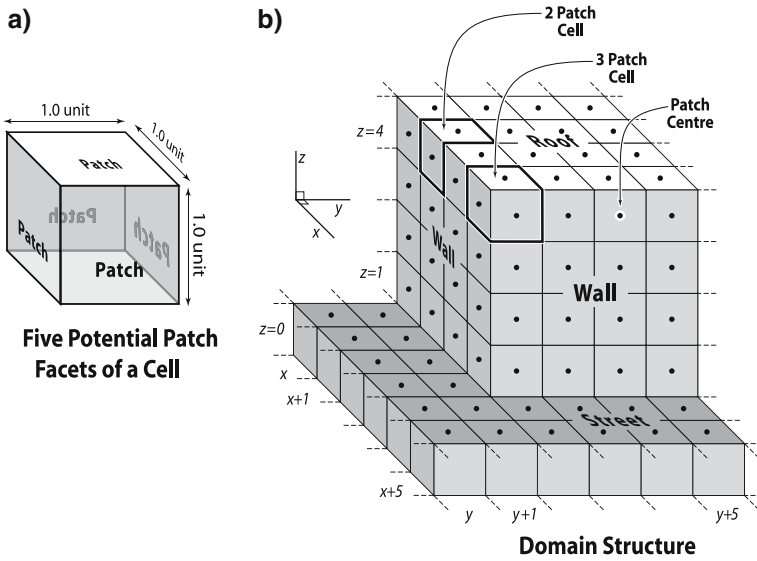
Fig. 1 Basic cubic cell and surface patch structure of TUF-3D
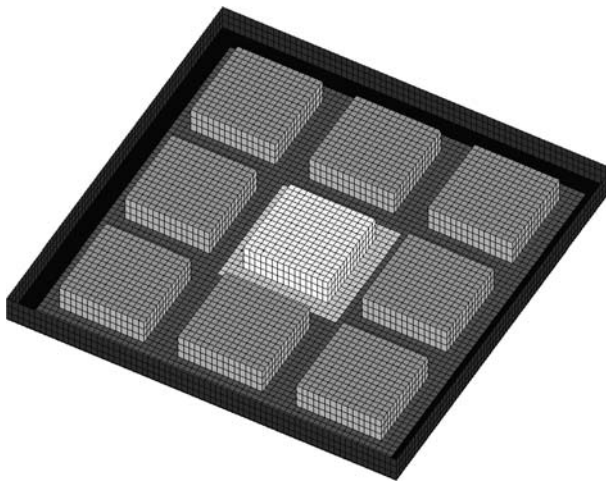
Fig. 2 An example TUF-3D domain with a bounding wall and the sub-domain S_d (chosen to coincide with the central urban unit) in lighter shades

cubic cells containing ambient air and those containing either the street layer or building interior. The ability to rotate the domain (i.e. the street orientation) any angle (η) from default alignment with the cardinal directions (i.e. $\eta = 0°$) is also included.

The model domain must be bounded radiatively in the horizontal to mimic continuous urban landscapes and therefore reduce the magnitude of radiative errors propagating inwards. Periodic boundary conditions may not be used because they require knowledge of the directionality of radiative 'flow' originating from the urban surfaces, which is only implicit in the radiosity-view factor method of radiative exchange used here (Ashdown 1994). Thus, the domain is surrounded by a wall of height equal to the

mean building height (rounded to the nearest whole number) that is separated from the original domain by a user-specified number of patches (Fig. 2), or by a default value based on a 3-D domain-average H/W ratio

$$\left[\frac{H}{W}\right]_{3D} = \frac{1}{2}\left(\frac{\lambda_c - 1}{1 - \lambda_p}\right) \tag{1}$$

where λ_c is the complete-to-plan area ratio, and λ_p is the roof-to-plan area ratio. Wall patches higher than the bounding wall can 'see' beyond the wall. As a first approximation, these patches interact radiatively with an external environment that has surface temperature and radiative properties that are user-prescribed or that are equal to those of user-selected patches within the domain.

A rectangular user-input sub-domain (S_d) is defined from $(x, y) = (x_1, y_1)$ to (x_2, y_2). Model outputs are computed over S_d, permitting flexibility in the output domain. Carefully chosen, e.g. over the central urban unit for regular building arrays (Fig. 2), the sub-domain provides representative results for the whole domain with little 'contamination' by the bounding wall. Tests indicate that domains of 3 by 3 (4 by 4) urban units yield domain-average albedo errors less than 2% (1%) relative to semi-infinite domains (not shown). Optimised versions of TUF-3D that are limited to specific types of geometries do not always require a bounding wall (see end of Sect. 2.1 below).

The approach taken in designing the sub-models focuses on those processes likely to most influence surface temperature distributions, and purposely ignores or employs a relatively simple approach for those processes unlikely to play a large role.

2.1 Radiation sub-model

All radiative reflection and emission is assumed perfectly diffuse, or Lambertian. This enables radiative exchange to be tracked with the use of view (or shape) factors, which determine the fraction of radiation emitted by a patch i incident on a patch j based on the size, orientation, and separation of the two patches. A ray tracing function determines whether each pair (i, j) of patches can 'see' each other. View factors for those patch pairs visible to one another are calculated with exact plane parallel analytical equations (Hottel and Sarofim, 1967; Siegel and Howell, 2001) combined with view factor algebra (Wu 1995). Surface patch sky view factors are also found during view factor computation with

$$\psi_{i,\text{sky}} = 1 - \sum_{j=1}^{n} \psi_{i,j} - \psi_{i,\text{external}} \tag{2}$$

where $\psi_{i,\text{sky}}$ is the sky view factor of surface patch i, $\psi_{i,j}$ is the view factor from patch i to patch j, $\psi_{i,\text{external}}$ is the view factor from patch i to external surfaces, and n is the total number of patches.

Direct shortwave radiation produces complex sunlit-shaded distributions over 3-D urban surfaces that are critical in the development of spatial distributions of surface temperature. A modified version of the Soux et al. (2004) ray tracing shading algorithm is adopted here. Vertical surface patches oriented in each of two shaded directions, as determined by the geometrical orientation relative to the solar azimuth angle, are immediately labelled as shaded. Subsequently, each remaining patch is divided into four equal sub-patches, which are tested to determine their sunlit/shaded status. The

division into shading sub-patches allows for more accurate solar energy input at lower model resolutions as well as for less spatial and temporal discontinuity in the surface sunlit distribution through the course of a day.

Longwave and shortwave reflection and absorption are modelled identically, but are initialised differently to properly account for the shading of direct solar, diffuse solar, and longwave emitted from both the sky and the urban surfaces. Initial incident sky-derived diffuse shortwave (longwave) radiative flux density at each surface patch i is determined from multiplication of patch i's sky view factor with the shortwave (longwave) sky diffuse radiative flux density, assuming isotropic sky radiance. Initial patch-level direct shortwave flux density is calculated based on the sun angle and patch orientation. Initial longwave radiative flux density emitted from each patch i is simply added to the first reflection of sky-derived longwave at that patch.

The radiation is reflected by canopy surfaces until the remaining unabsorbed radiation is below a user-defined threshold; such an iterative approach is taken in order to avoid the memory requirements of an exact matrix solution. A reflection event consists of each surface patch i reflecting a fraction (α_i for shortwave, $1 - \varepsilon_i$ for longwave) of the total incident radiation from all other visible patches (in the whole domain) during the previous reflection

$$R_i^{q+1} = \alpha_i \sum_{j=1}^{n} \psi_{j,i} R_j^q, \qquad (3)$$

where R_i^{q+1} is the radiation reflected by patch i at reflection $q + 1$ and R_j^q is the radiation reflected by patch j at reflection q. Patch absorption is calculated analogously. A minimum of two reflections is performed, and reflections continue thereafter until the changes in *both* sub-domain averaged shortwave albedo *and* longwave reflectivity between reflections are less than $\Delta\alpha_D$. The default $\Delta\alpha_D$ is $0.001(1 - \lambda_{pH})$, where λ_{pH} is the building-plan area fraction at the mean building height, z_H. In direct analogy to the shortwave albedo calculation, sub-domain average longwave reflectivity is determined by dividing the total radiation *reflected* (not emitted) upwards by the total incident radiation from all sources (i.e. including emission from the domain surfaces in addition to the sky, unlike shortwave radiation).

Since much urban climate research still takes place in the context of the urban canyon, a version of TUF-3D that is optimised for two-dimensional (2-D) scenarios, TUF-2D, is created by imposing horizontal homogeneity in the y-dimension and therefore only solving Eq. 3 for those patches i with a chosen y-value. Furthermore, regular 3-D arrays (i.e. arrays composed of one repeating urban unit) are modelled with an optimised version of TUF-3D that imitates periodic boundary conditions by solving Eq. 3 only for patches in the central urban unit, and setting radiative and energy balance exchanges of all other patches equal to the corresponding patch within the central urban unit. In both cases computational savings are generally so substantial that increased horizontal extension of the domain eliminates the need for a bounding wall. The different versions of the model are collectively referred to as "TUF".

2.2 Conduction sub-model and surface temperature

The solution of the energy balance for each surface patch at each timestep requires the calculation of heat conduction and the associated temperature profile within the patch substrate. One-dimensional conduction within the patch substrate is bounded

by surface energy exchanges at the patch surface and by the internal building energy exchanges or a deep-soil temperature at the substrate base. A version of the one-dimensional (1-D) heat conduction equation that permits variable layer thickness and thermal conductivity is solved by finite differences for each patch (Masson 2000)

$$T_b^{m+1} - T_b^m = \frac{\Delta t}{C_b \Delta x_b} (\gamma (G_{b-1,b}^{m+1} - G_{b,b+1}^{m+1}) + (1 - \gamma)(G_{b-1,b}^m - G_{b,b+1}^m)), \quad (4)$$

where T_b, C_b, and Δx_b are the temperature, volumetric heat capacity, and depth of layer b, respectively, Δt is the timestep, m is the timestep index, γ is the degree of implicitness (i.e. $\gamma = 0$ is explicit, $\gamma = 1$ is implicit), and $G_{b,b+1}^m$ is the conductive heat flux between layers b and $b + 1$ at timestep m, calculated from

$$G_{b,b+1}^m = k_{b,b+1} \frac{(T_b^m - T_{b+1}^m)}{\frac{1}{2}(\Delta x_b + \Delta x_{b+1})}. \quad (5)$$

The thermal conductivity between layers b and $b + 1$ of differing thicknesses, $k_{b,b+1}$, is approximated by analogy to the theory of electrical circuits, whereby conductance reciprocals (i.e. resistances [m^2 K W^{-1}]) add in series (Masson 2000). The T_b^{m+1}, for $b = 1$ (the surface layer) to p (the deepest layer), are solved at each time step for each patch by matrix decomposition and back-substitution of the tridiagonal matrix resulting from Eq. 4 (Jacobson 1999).

A version of the approach used by Arnfield (1990) to model the surface boundary condition (i.e. the surface temperature) is used. The energy balance at the surface for a given patch i, omitting the 'i' subscripts, reads

$$(1 - \alpha) K{\downarrow}^{m+1} + \varepsilon \left(L{\downarrow}^{m+1} - \sigma (T_{\text{sfc}}^{m+1})^4 \right) - h^{m+1} (T_{\text{sfc}}^{m+1} - T^{m+1}(z))$$

$$- \frac{k_1 (T_{\text{sfc}}^{m+1} - T_1^m)}{\frac{1}{2} \Delta x_1} = 0, \quad (6)$$

and is solved for the surface temperature at the next timestep (T_{sfc}^{m+1}). All other non-radiative variables in Eq. 6 are calculated prior to its solution. Equation 6 is solved by Newton's method until the patch surface temperature differs less than 0.001 K between iterations. When multiple patches are present that interact radiatively, such as within an urban canopy, an additional layer of iteration is added (Arnfield 1990). That is, the longwave emission and multiple reflections are solved anew with the newly calculated patch surface temperatures, followed by the recalculation of Eq. 6 with updated $L{\downarrow}_i^{m+1}$ for each patch i (which is a function of the $T_{\text{sfc},j}^{m+1}$ from other patches j that are viewed), and so on until system equilibrium is achieved. The latter is attained (for modelling purposes) when no single patch surface temperature changes by more than a user-specified amount between iterations (default: $\Delta T_{\text{crit}} = 0.01$ K).

The surface boundary condition is specified as the conduction *flux density* used in Eq. 6 regardless of the γ value. Thus, Eq. 4 for layer 1 is

$$T_1^{m+1} - T_1^m = \frac{\Delta t}{C_1 \Delta x_1} (G_{\text{sfc},1}^{m+1} - \gamma G_{1,2}^{m+1} - (1 - \gamma) G_{1,2}^m) \quad (7)$$

with $G_{\text{sfc},1}^{m+1}$ equal to the last term on the left side of Eq. 6.

The boundary condition at the base of the deepest substrate layer is simply one of conductive exchange with a constant 'deep-soil' (T_D; streets) or 'internal' (T_{INT};

roofs and walls) temperature. An additional resistance to heat transfer of $\Omega_{INT} = 0.123\,\mathrm{m}^2\,\mathrm{K}\,\mathrm{W}^{-1}$ is added for conduction at inner wall and roof surfaces because radiative and convective heat transfer between the building interior and inner wall and roof surfaces encounters more resistance than that present between two solids in direct thermal contact (Masson et al. 2002). Additionally, an incremental-adjustment of the internal building temperature is added based on the average patch internal layer temperature, after Masson et al. (2002).

2.3 Convection sub-model

In order to effectively model convection from surfaces the amount of mechanical energy in the flow adjacent to the surface must be estimated. Energy balance models that resolve the urban canopy layer have typically employed either a single effective within-canyon wind speed (Masson 2000; Kusaka et al. 2001), or a vertical diffusion approach (Martilli et al. 2002; Kondo and Kikegawa, 2003) that yields a vertical profile of wind speed and in some cases turbulence. Additionally, the thermal energy of the flow must be modelled, both to determine stability effects on vertical turbulent transport, and to estimate the surface–air thermal gradient that controls convective heat transfer. The former group of models estimates a mean within-canyon temperature, while the Martilli et al. (2002) model calculates a vertical profile of temperature. A more accurate and computationally expensive approach would involve implementation of a computational fluid dynamics (CFD) model. However, forcing of surface temperature by the evolution of the sunlit-shaded distribution and its modulation by surface material properties is likely to be significantly more important than forcing by the distribution of convection across and between facets. Thus, an empirically based (i.e. non-CFD) approach to convection is taken in the initial version of the model and the quality of the surface temperature results is investigated.

Although the observations and the theoretical basis necessary to effectively parameterise 3-D convection without employing an explicit flow model are relatively incomplete, it is nevertheless a reasonably successful approach taken in many urban canopy layer models that do not resolve the sub-facet scale radiatively (Masson 2000; Kusaka et al. 2001), and in some that do (e.g. Arnfield and Grimmond 1998). Here, convection is treated with a formulation that is essentially an adaptation of the facet-average approach taken by Masson (2000). Advective horizontal exchanges are neglected, which is a reasonable approximation at larger scales if the modelled domain is assumed to be part of an extensive area of similar land cover. It may also be a reasonable approximation at the sub-facet scale given the generally well-mixed nature of canopy layer air, but this question awaits a more physically complete approach.

2.3.1 Wind speed profile

The general framework employed for parameterization of the wind speed profile in the roughness sub-layer (RSL) is the logarithmic 'law'. Although the assumption of a constant-stress layer is not always borne out by observations (Rotach 1993), previous models requiring parameterization of the RSL have implicitly assumed a log profile (e.g. Masson 2000; Kusaka et al. 2001; Harman et al. 2004). Thus

$$U(z) = U_a \ln\left(\frac{z - z_d}{z_{0\mathrm{town}}}\right) \bigg/ \ln\left(\frac{z_{\mathrm{ref}} - z_d}{z_{0\mathrm{town}}}\right), \quad (z \geq z_H), \tag{8}$$

where $z_{0\text{town}}$ is the overall domain roughness length for momentum, z_d is the displacement height, and z_{ref} is the height of the forcing wind (U_a) above street level; $z_{0\text{town}}$ and z_d are user-specifed or calculated from Macdonald et al. (1998).

Exponential profiles have successfully modelled vertical velocity profiles through vegetation canopies (Cionco 1965) and simple urban arrays (Macdonald 2000; Coceal and Belcher 2004). Here it is assumed that convection is dependent on the wind *speed* adjacent to surfaces, not the velocity, for temporal and spatial averages. For example, skimming flow generally exhibits negative average velocities (relative to above-canopy flow) but significant average speeds near ground level. Nevertheless, one full-scale ($H/W \approx 1$) set of observations suggests that an exponential wind speed profile is appropriate (Rotach 1995). In fact, although Rotach's study does not measure below $z/z_H \approx 0.4$, the wind speed appears to become constant with height below $z/z_H \approx 0.7$ (Fig. 3). He also finds that there is rarely a significant difference between the wind speed at the canyon centre and that midway between the canyon centre and the wall. Masson (2000) relies on Rotach's observations in assuming an exponential wind profile within the canyon.

For lack of additional experimental data at other flow regimes, an exponential canopy wind-speed profile is employed here. It is calculated based on the following condition

$$U\left(\frac{z_H}{2}\right) = U(z_H) \exp\left(\frac{-\lambda_f}{2(1-\lambda_p)}\right), \tag{9}$$

where the frontal area index (λ_f) is input by the user or defined based on Raupach (1992). Equation 9 gives very similar results to Kusaka et al. (2001) for a range of typical H/W values, but is significantly higher than Masson (2000) for $H/W < 2.5$.

It is found that a canopy profile of the form

$$U(z) = A + B\exp(Cz), \quad (z < z_H), \tag{10}$$
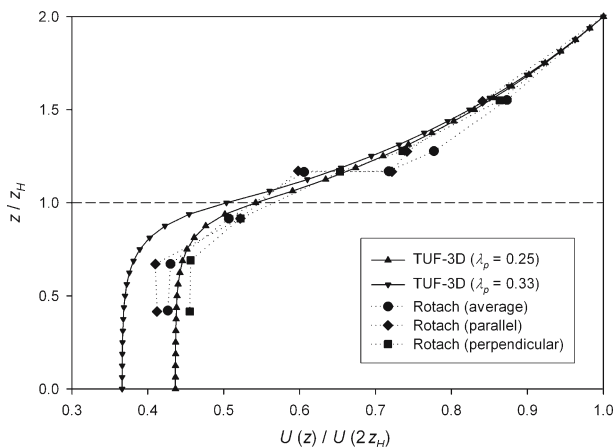
Fig. 3 The TUF-3D wind-direction averaged wind speeds for cubic arrays at two plan areal fractions, $\lambda_p = 0.25$ and $\lambda_p = 0.33$, corresponding to $H/W \approx 1$ as defined by the ratio of building-height to street-width and by Eq. 1, respectively. Rotach's (1995) $H/W \approx 1$ full scale results are included for comparison (average = overall average; parallel = wind direction parallel to canyon axis ($\pm 30°$); perpendicular = wind direction perpendicular to canyon axis ($\pm 30°$))

may be used to satisfy Eq. 9 while also matching the zeroth and first derivatives of the canopy and above-canopy profiles at $z = z_H$. Here, A, B, and C are time-dependent parameters, and a system of three equations and three unknowns is generated. The coefficient C is solved iteratively with the bisection method and then A and B are solved by substitution. The formulation compares well with the results of Rotach (1995) through both the canopy and above-canopy layers (Fig. 3). Furthermore, it yields realistic variations through a range of typical packing densities, and approaches zero for high λ_p. The asymptotic approach of canopy wind speed to $U(z_H)$ for low λ_p correctly results in greater canopy ventilation, but the actual wind-speed profile may be less realistic (i.e. one might expect a log profile down to $z = z_d$, where z_d can be quite small relative to z_H for low λ_p). However, such built densities are less common in practice. Overall, the canopy wind parameterization yields similar canopy (canyon) speeds at $0.5z_H$ to Kusaka et al. (2001) and to Masson (2000) (except for low H/W), and additionally incorporates increased speeds near the canopy top and continuity with the above-canopy wind profile.

2.3.2 Temperature profile and canopy energy budget

The temperature profile is similar to the wind profile except that canopy temperature is constant (i.e. for $z < z_H$), which allows for the calculation of a single explicit canopy-air energy budget. This assumption is based on several observational studies (Nakamura and Oke 1988; Arnfield and Mills 1994; Rotach 1995) and is employed in several canopy-layer models (Mills 1997a; Masson 2000; Kusaka et al. 2001). The above-canopy logarithmic temperature profile ($T_{\log}(z)$) between T_{can} at $z = z_H$ and T_a at $z = z_{ref}$ is formulated similarly to the above-canopy wind-speed profile (Eq. 8), by rearranging the bulk heat transfer coefficient equation of Louis (1979). z_{0town} is used as the roughness length for momentum and also for heat because of the relative efficiency of canopy-air to boundary-layer exchanges (Lemonsu et al. 2004). Above-canopy logarithmic temperature profiles are implicit in the models of Masson (2000) and Kusaka et al. (2001), and the present version agrees with observations from the BUBBLE (Rotach et al. 2005) intensive observation period (IOP) at the Sperrstrasse site in Basel ($H/W \approx 1$), June 20 to July 13, 2002 (Fig. 4).

The canopy air temperature is calculated by means of an explicit energy budget of the volume of air below $z = z_H$ and within the sub-domain (S_d):

$$T_{can}^{m+1} = T_{can}^m + \left[\frac{\Delta t (H_{can}^{m+1} - H_{top}^{m+1})}{c_{air,H}^{m+1}} \right]_{S_d}, \qquad (11)$$

where $c_{air,H}$ [$\text{J m}^{-2}\,\text{K}^{-1}$] is the average heat capacity of air per unit plan area below z_H, H_{can} is the sum of the convective fluxes from all the patches below $z = z_H$, divided by the canopy-air-plan area ratio at height z_H, $1 - \lambda_{pH}$, and H_{top} is the convective flux density of sensible heat across the canopy 'top' (positive upwards), a fictional surface at $z = z_H$. Here,

$$H_{top}^{m+1} = h_{top}^{m+1}(T_{can}^m - T_a^{m+1}), \qquad (12)$$

where h_{top} is the convective heat transfer coefficient, and is calculated with the Mascart et al. (1995) stability coefficients with z_{0town} used as the roughness length for heat.
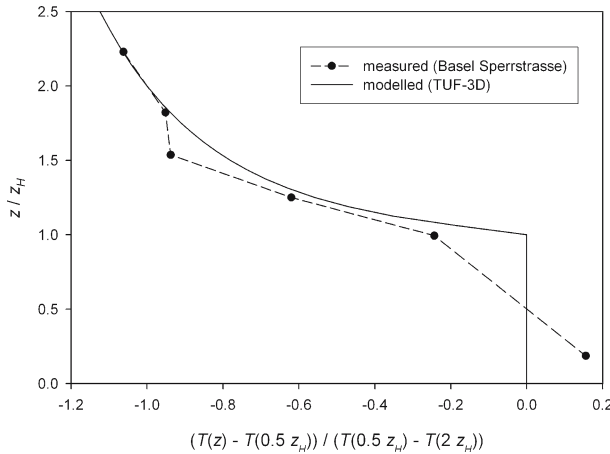
Fig. 4 Temperature profiles normalized by the temperature difference between $0.5z_H$ and $2z_H$. The TUF-3D profile is for $\lambda_p = 0.51$, $\lambda_f = 0.22$, and a building-height to street-width ratio of 1, corresponding approximately to the local-scale geometry at the Sperrstrasse site in Basel during BUBBLE (Rotach et al. 2005). The measured Sperrstrasse profile is an average over all observations during the BUBBLE IOP (24 days)

The complete vertical air temperature profile is expressed as

$$T(z) = \begin{cases} T_{\log}(z), & (z \geq z_H); \\ T_{\text{can}}, & (z < z_H). \end{cases} \tag{13}$$

2.3.3 Patch heat transfer coefficients

As in Masson et al. (2002) and Martilli et al. (2002), transfer from horizontal surfaces is treated with a Monin–Obukhov similarly theory (MOST) formulation, accounting for stability effects, while the transfer from vertical surfaces is based on wind-tunnel measurements of forced convection from flat plates (e.g. Rowley and Eckley 1932; Rowley et al. 1930a, b; Clarke 1985). The application of MOST to finite urban facets is disputed, but it is applied here in the absence of an alternative (e.g. Martilli et al. 2002).

Convection from a horizontal patch i of any height, including all roof and road patches, follows the typical formulation

$$H_i = h_i(T_{\text{sfc},i} - T(z_{\text{horz},i})), \tag{14}$$

where $z_{\text{horz},i} = z_i + L_{h,i}$, z_i is the height of the patch centre, and $L_{h,i}$ is the patch forcing height, defined analogously to Harman et al. (2004)

$$L_{h,i} = \begin{cases} 0.1\, z_H, & (\text{streets}) \\ 0.1\, L_R, & (\text{roofs}) \end{cases} \tag{15}$$

where L_R is a domain-average roof length, and $L_{h,i}$ approximates the facet-average internal boundary-layer height. Airflow near streets exhibits greater flow regime dependence than that above roofs and so a value linked to z_H is chosen for simplicity (Harman et al. 2004). Horizontal patch heat transfer coefficients h_i are calculated using the stability coefficients of Mascart et al. (1995) and an effective wind speed,

$U_{\text{eff}}(z)$, which, for non-roof patches, includes an additional term to account for the thermal production of turbulence within the canopy during convective conditions (Lemonsu et al. 2004). The Mascart et al. (1995) stability functions are calculated with $z_{0m}/z_{0h} = 200$ (by default), the upper limit of their functions' validity. Voogt and Grimmond (2000) find much larger z_{0m}/z_{0h} ratios on the order of 10^9. In practice, this suggests that the horizontal h_i may be overestimated here by approximately 150%.

Convection from walls follows the same general formulation (i.e. Eq. 14), with two exceptions: the wind and temperature forcing the convection at a given patch i are taken at the wall patch's height, z_i, and the h_i are calculated based on a flat plate forced convection relationship for vertical patches,

$$h_i = r_{w,i} (11.8 + 4.2\, U_{\text{eff}}(z_i)) - 4.0, \tag{16}$$

where $r_{w,i}$ is the user-input wall patch roughness relative to the default of 1.0 for concrete (ASHRAE 1981).

Equation 16 is simply a reduction of the Rowley et al. (1930a, b) formulation by $4\,\text{W}\,\text{m}^{-2}\,\text{K}^{-1}$ based on information presented in Cole and Sturrock (1977); that is, there is a radiation component included in wind-tunnel derived convection coefficients, and its magnitude is on the order of $4\,\text{W}\,\text{m}^{-2}\,\text{K}^{-1}$. Furthermore, Eq. 16 yields h values that fall between the original Rowley et al. (1930b) formulation used by Masson (2000) and other commonly used formulations in urban energy balance models (e.g. Clarke 1985, used in Martilli et al. 2002) for common near-surface wind speeds ($<15\,\text{m}\,\text{s}^{-1}$).

3 Testing the radiation sub-model

Tests are performed on both the multiple reflection and the solar shading routines in a cavity-type geometry to ensure energy conservation. Subsequently, comparisons are made between Aida's (1982) observations and the simulated effective albedos of urban canyons and 3-D block arrays. Finally, the Kanda et al. (2005b) scale model block array effective albedo measurements are simulated.

Raster surfaces of finite resolution combined with ray tracing steps of finite frequency result in imperfect energy receipt calculation by the shading routine. That is, the number of sunlit patches will either overestimate or underestimate the total input $K\!\downarrow_{\text{dir}}$, unless the actual sunlit-shaded border falls precisely along the intersections of surface patches throughout the domain. Fractional errors are larger for zenith angles $\phi > 65°$; however, low radiative fluxes at these angles will serve to offset the impacts on the energy balance. The magnitude of error reduction decreases as the resolution is increased (Fig. 5), where resolution simply refers to the number of patches across a surface in a single dimension. A cavity with 4-patch resolution in each dimension has a mean absolute percent shading error of 5.2%, while resolutions 6 and 8 have percent errors of 3.2 and 2.7%, respectively. Multiple reflection errors are substantially smaller.

TUF simulated canopy effective albedo is compared to the December 3, 1977 and June 15, 1978 clear sky "scrap and build" scale model albedo measurements of Aida's (1982) on a building roof in Yokohama, Japan. Effective albedo is calculated based on the radiation reflected upwards by one urban unit. Aida's (1982) measured global $K\!\downarrow$ and $K\!\uparrow$ above a scale model of "infinite" concrete canyons with facet albedos of approximately 0.40, and $z_H = x_W = x_L = 0.15\,\text{m}$ ($\lambda_p = 0.50$, $H/W = 1$). Both
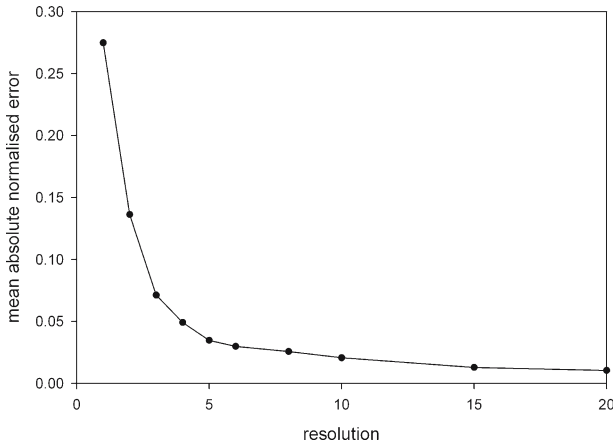
Fig. 5 Mean absolute normalised error in cavity average direct solar receipt as a function of resolution. Values at a given resolution are averages over all azimuth and zenith angles, both in 5° increments

north–south and east–west oriented canyons and a regular cubic block array ($\lambda_p = 0.25$) were used by scrapping and rebuilding in turn as the day progressed.

Solar angles in TUF are calculated based on Iqbal (1983) and Stull (2000), while Rayleigh scattering, ozone and water vapour absorption, and aerosol scattering and absorption are modelled using a broadband parameterization model developed by several authors and presented in Chapter 7 of Iqbal (1983). Clear skies with a relatively turbid atmosphere are assumed, and the average surface albedo of Yokohama (for the contribution of multiple reflection between the surrounding city and the atmosphere to $K\!\downarrow_{dif}$) is taken to be 0.20 (Sievers and Zdunkowski 1985). Monthly climatological mean temperatures and dewpoints for Yokohama are employed, as in Arnfield (1988), allowing for the estimation of precipitable water with methods reviewed in Iqbal (1983).

Based on their calculations of direct/diffuse partitioning, and on flat concrete measurements made by Aida's (1982), Sievers and Zdunkowski (1985) derived an expression for the albedo of the flat concrete used in the experiment as a function of ϕ and direct/diffuse partitioning. They found that using this expression for the roof albedo (α_R) instead of $\alpha_R = 0.40$ markedly improves their results. Masson (2000) also varies α_R but does not give details, while Arnfield (1988) uses an α_R based on Aida's (1982) flat concrete measurements and estimates $\alpha_W = \alpha_r = 0.405$ based on a zenith angle averaging procedure, where α_W and α_r are the wall and street albedos, respectively. Sievers and Zdunkowski (1985) obtained little improvement by applying similar methods to α_W and α_r. Thus, both $\alpha_R = 0.40$ and the Sievers and Zdunkowski (1985) α_R expression are used here for comparison purposes, but α_W and α_r are held constant at 0.40.

TUF's performance relative to Aida's (1982) scrap and build measurements is compared with the performance of other similar models in Table 1. TUF-2D canyon results have very similar accuracy to those of Sievers and Zdunkowski (1985). Both models fare less well in winter, but show improvement with the Sievers and Zdunkowski variable roof albedo. The Masson (2000) results are in the same range, while Arnfield (1988) results are exceptionally good for a winter–summer average, which

Springer

Table 1 Mean absolute differences in effective albedo between various modelling studies and the scrap and build measurements of Aida's (1982)

Study	Canyons (N–S and E–W)		Cubes	
	June 15, 1978	Dec 3, 1977	June 15, 1978	Dec 3, 1977
SZ85	0.014	0.046	–	–
SZ85[a]	0.015	0.020	–	–
Masson (2000)	0.000–0.015[b]	–	0.022–0.044[b]	–
Arnfield (1988)	0.014[c]		0.033[c]	
TUF-3D	0.012[d]	0.046[d]	0.006	0.027
TUF-3D[a]	0.009[d]	0.022[d]	0.007	0.014

[a] With SZ85 variation in roof albedo
[b] Approximate range of differences compared to Aida's standing measurements on July 27–28, 1978, and June 22, 1979
[c] June 15 and December 3 results combined; the author uses a canyon averaging procedure for cube results
[d] TUF-2D
SZ85 = Sievers and Zdunkowski (1985)

may relate to the different choices of α_R and $\alpha_r = \alpha_w = 0.405$ used in his simulations. The cube results demonstrate the superiority of TUF-3D for 3-D geometries. The Masson (2000) and Arnfield (1988) 2-D models significantly and consistently underestimate the effective albedo, likely because they ignore the increased sky view factors of intersections. TUF-3D disagreement with the Aida observations is larger in winter (i.e. for low ϕ). However, errors in Aida's measurements are also likely to be larger at higher ϕ.

A more recent observational and modelling study of effective albedo of regularly-spaced cube arrays (Kanda et al. 2005b) extends observations through one additional season (autumn) and two additional building plan area fractions ($\lambda_p = 0.44, 0.69$), accounting for a greater range of λ_p to sun-angle combinations. Kanda et al. (2005b) compare these observations with results from several models, including the highly-accurate model (HM) of Kawai and Kanda (2003), which has a similar structure to the TUF-3D radiation sub-model.

TUF-3D inputs are matched to those used by Kanda et al. (2005b), while incoming solar is calculated as before. All patches have variable albedo given by an expression Kanda et al. (2005b) derived for the albedo of their concrete as a function of ϕ, with ϕ replaced by the angle between the patch normal and the sun angle for vertical patches (i.e. wall patches). The albedo of the central urban unit is extracted for comparison. Observations and HM results are extracted from Kanda et al. (2005b) in such a manner as to avoid an excessive number of data points. Thus, some detail of high temporal resolution (approximately $\Delta t \leq 0.5$ h), whether real or noise, is manually filtered out, permitting only a comparison of the main trends.

TUF-3D agrees well with the HM results (Fig. 6), particularly for smaller ϕ (i.e. in summer, and closer to solar noon). Both models perform well relative to observations but tend to overestimate effective albedo at higher building packing densities. Kanda et al. (2005b) suggest that this is because the radiometer is placed above a street intersection, and therefore it underestimates the true albedo because canopy (intersection) albedo is lower than roof albedo. This preferentially affects observations at higher packing densities (Kanda et al. 2005b), and therefore may explain much of the
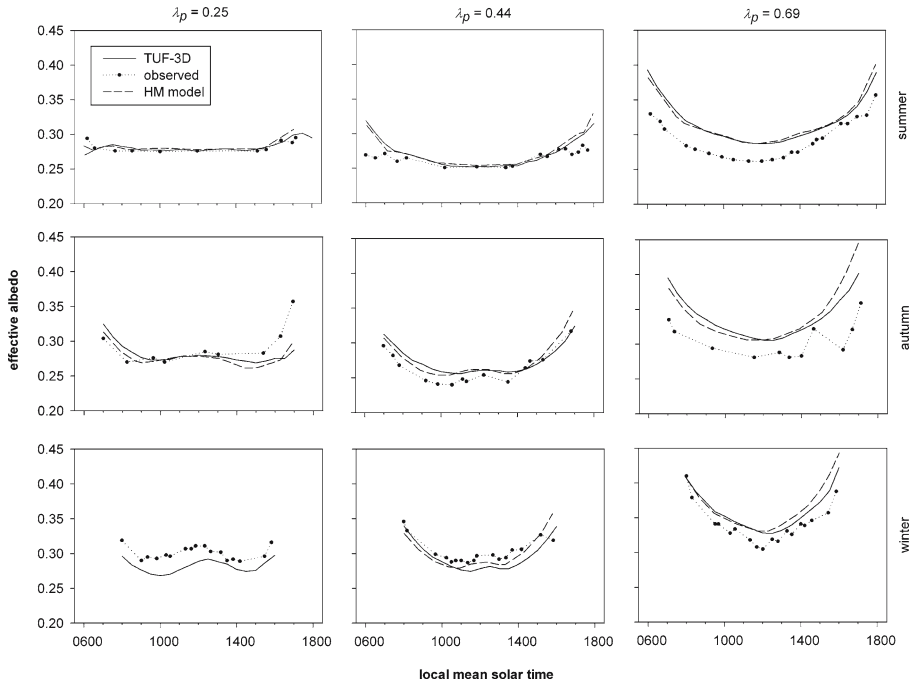
Fig. 6 Comparison of modelled and measured cube array effective albedo as a function of local time for three different cube densities (λ_p) and three seasons. Observed and HM model values are extracted from Kanda et al. (2005b). See text for details

model–observation discrepancy at $\lambda_p = 0.69$. Larger model–observation disagreement at higher ϕ (i.e. early morning and late afternoon, and winter) is probably a combination of larger radiometer errors and larger model shading errors at these ϕ angles.

4 Testing the conduction sub-model

Comparisons of the conduction sub-model with observations are limited to cooling scenarios when solar forcing is absent, due to a lack of datasets in the literature. TUF conduction sub-model results are first corroborated for a flat surface (i.e. 1-D conduction for a single patch) with the 12-h cooling simulations for three different surface types (moist soil, dry soil, and asphalt) performed by Arnfield (1990), who used an almost identical conduction scheme. Subsequently, the urban canyon night-time cooling measurements of Nunez and Oke (1977), which have become a common test dataset for the coupled radiative-conductive portions of urban climate models (Johnson et al. 1991; Masson 2000; Kusaka et al. 2001), are used. Nunez and Oke measured nocturnal *near-surface air* temperature and net longwave at the midpoints of each of three facets of an asymmetrical canyon. Unlike other modelling studies, the current approach includes the wall asymmetry, with both the floor and the west-facing (west) wall nine patches wide/high, and the east-facing (east) wall seven patches high.
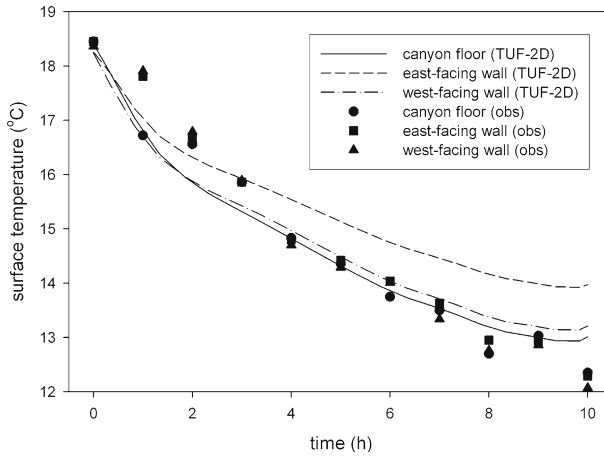
Fig. 7 Evolution of Nunez and Oke (1977) observed near-surface temperature and TUF-2D modelled surface temperature of canyon facets during the evening of September 9/10, 1973, in the Grandview District of Vancouver. All measurements and model results are for the midpoints of each facet

It is assumed that nighttime convective exchanges are small and therefore that surface temperatures are well approximated by the measured near-surface air temperatures.

Thermal conductivities (k), heat capacities (C) and wall thickness are from Masson (2000), while streets are 0.30 m thick. Initial surface and constant deep temperatures and surface emissivities are from Johnson et al. (1991). The initial temperature profile varies with depth such that the initial conductive heat flux is constant with depth and conduction balances surface radiative exchange. Introduction of an additional 'spin-up' hour of simulation to better initialise the substrate temperature profiles makes little difference to the results. $L\downarrow$ at the canyon top is not measured and is therefore estimated using Prata (1996) with hourly temperature and humidity data from the Vancouver airport. $K\downarrow$ is included using the scheme described in Sect. 3 and slightly affects results for both the first hour and the last half-hour of the simulation, while convection is not included in order to focus on the conduction scheme performance.

Temperatures compare well with observations over the period of simulation (Fig. 7), tending to underestimate in the early hours and demonstrate better agreement later on with the exception of the east-facing wall. Modelled inter-facet differences resulting from differences in facet ψ_{sky} are not apparent in the observations or in the other modelling studies (which employ symmetrical canyons). Introduction of convection into the present TUF-2D simulation reduces the divergence of the east wall temperature by half (not shown). However, low wind speeds for the second half of the simulation period suggest mechanical convection is not strong ($\overline{U_a} < 0.5\,\mathrm{m\,s^{-1}}$ at the airport). The fact that the measurements are near-surface *air* temperatures may play a role.

Overall, agreement is good, with mean (maximum) hourly absolute differences for the floor, east-, and west-facing walls of 0.3°C (0.7°C), 0.9°C (1.9°C), and 0.4°C (1.1°C), respectively. Net longwave exchange also demonstrates reasonable model to observation agreement, with mean (maximum) absolute differences of 6.3 (10.9), 2.4 (4.6), and 4.3 (6.9) W m^{-2} for the floor, east and west walls, respectively. The tests performed here show that the conduction scheme performs adequately both for a single column and in a 2-D geometry when combined with the radiation scheme.

5 Full model tests

Typically, output from an urban energy balance model is compared both statistically and graphically to observed fluxes and surface and/or air temperatures (e.g. Masson et al. 2002). Here, such comparisons are performed for clear summertime cases, which exhibit the strongest solar forcing and therefore present the most rigorous test of the model. Sensitivity testing of the complete model is not shown here for the sake of brevity.

Modelled *apparent* surface temperatures are employed in many comparisons with observations since they more closely approximate infrared thermometer (IRT) apparent surface temperatures than do modelled surface temperatures that result from the solution of the surface energy balance. Apparent surface temperatures include the surface emissivity and multiple reflection (together, effective emissivity) effects that are inherent in the observations. A sensitivity test of the Laguerre–Gauss quadrature method of converting between surface temperature and radiation emitted in the 8–14 μm range (i.e. the IRT wavelength range) suggests that the use of the Stefan–Boltzmann (i.e. wavelength-integrated) equation to determine surface temperature introduces only minor errors for a range of component surface temperature and view factor combinations. Therefore, conversions between modelled radiation and surface temperature quantities employ the Stefan–Boltzmann equation, and apparent surface temperature is defined here, for patch i, as

$$T_{\mathrm{app},i} = \left(\varepsilon_i T_{\mathrm{sfc},i}^4 + \frac{(1 - \varepsilon_i) L{\downarrow}_i}{\sigma} \right)^{0.25}. \tag{17}$$

Model to observation comparison is performed purely in an operational sense, that is, only an assessment of model accuracy is undertaken (Willmott et al. 1985). Mean bias error (MBE), root-mean-square error (RMSE), and goodness-of-fit (r^2) are reported here to quantify bias, absolute error and model–observation covariance, respectively.

5.1 Vancouver light industrial (facet-average comparison)

The Vancouver Light Industrial (LI) site is an ideal test for the TUF-3D model in several respects. It is characterised by a high density of 1–3 story buildings of mainly rectangular footprint, roofs are primarily flat, and there is a distinct lack of vegetation (<5% of plan area; Masson et al. 2002). Airborne thermal remotely sensed radiative surface temperatures were obtained at three times (local mean solar time, or LMST) on August 15, 1992: 0850-0950 (flight 1), 1235–1320 (flight 2), and 1555–1635 (flight 3) (Voogt and Oke 1998). Concurrently, truck mounted thermal remote sensors measured temperatures of walls and streets and instrumented towers, at both the LI site (28.5 m for fluxes, 9 m for meteorological variables) and the nearby Sunset residential site, measured radiative and turbulent fluxes, air temperature, wind speed and direction, and other meteorological quantities. Furthermore, August 15, 1992 was a clear day, yielding well-defined sunlit-shaded patterns over the 3-D surface. However, the development of a strong sea breeze as early as mid-morning contributed undesired complexity. Further detail is available in Voogt and Grimmond (2000).

As an objective means of specifying the input parameters, the Masson et al. (2002) parameters are employed (Table 2a, b). Rather than attempting to replicate some small fraction of the LI site geometry, a simple 5 by 5 array of buildings that neverthe-

Table 2 (a) Parameters employed in the Vancouver LI and Basel Sperrstrasse simulations, including model specific geometry and integration parameters. (b) Thermal parameters employed in the Vancouver LI and Basel Sperrstrasse simulations

Parameter	Vancouver	Basel
a:		
Geometric		
λ_p	0.51	0.53
z_H (m)	5.79	14.6
λ_c	1.41	2.18
$z_{0\text{town}}$ (m)	0.35	1.73
Roof $z_{0m}(m)$	0.15	0.15
Street z_{0m} (m)	0.05	0.02
z_{ref} (m)	8.5	31.8
$\eta(°)$	3.0	70.0
Model specific		
l_p (m)	0.965	1.46
Street width[a]	12	8
Building height[a]	6	10
Building length[a]	30 by 30	9 by 120
Radiative		
α_R	0.12	0.12
α_r	0.08	0.11
α_W	0.50	0.30
ε_R	0.92	0.91
ε_r	0.95	0.92
ε_W	0.90	0.85
Initial values		
$T_R(°C)$	12.0	14.0
$T_r(°C)$	20.0	24.5
$T_W(°C)$	19.0	21.5
$T_{\text{INT}}(°C)$	22.0	22.0
$T_D(°C)$	20.0	20.0

Parameter	Unit	Simulation	Layer 1	Layer 2	Layer 3	Layer 4
b:						
Roofs						
Δx	m	Vancouver	0.015	0.015	0.010	0.030
k	$\text{W m}^{-1}\,\text{K}^{-1}$	Vancouver	1.40	1.40	0.03	1.51
C	$\text{MJ m}^{-3}\,\text{K}^{-1}$	Vancouver	1.76	1.76	0.04	2.21
Streets						
Δx	m	Vancouver	0.050	0.200	0.500	0.500
		Basel	0.020	0.030	0.100	0.500
k	$\text{W m}^{-1}\,\text{K}^{-1}$	Vancouver	0.82	2.10	0.40	0.40
		Basel	0.84	0.84	0.93	0.28
C	$\text{MJ m}^{-3}\,\text{K}^{-1}$	Vancouver	1.74	2.00	1.40	1.40
		Basel	1.92	1.92	1.55	1.35
Walls						
Δx	m	Vancouver	0.030	0.070	0.070	0.030
		Basel	0.009	0.034	0.085	0.017
k	$\text{W m}^{-1}\,\text{K}^{-1}$	Vancouver	1.51	0.67	0.67	1.51
		Basel	1.12	1.12	1.12	0.28
C	$\text{MJ m}^{-3}\,\text{K}^{-1}$	Vancouver	2.11	1.00	1.00	2.11
		Basel	1.74	1.93	1.93	1.49

Sources: Oke (1987), Mills (1993), Voogt and Oke (1997), Masson et al. (2002), Rene Dupuis (personal communication 2003), Christen and Vogt (2004)
[a] In numbers of patches

less preserves the local-scale geometrical ratios (Table 2a), as presented in Voogt and Oke (1997) and Masson et al. (2002), is employed. Forcing data (T_a, U_a, P_a, e_a, $K\downarrow$) required to run the model is extracted from tower measurements at the LI and Sunset residential sites. $K\downarrow_{dir}$ /$K\downarrow_{dif}$, ϕ, δ, and $L\downarrow$ are calculated as in Sects. 3 and 4. Simulations begin at 0300 LMST to allow model equilibration prior to the onset of solar forcing at approximately 0500 LMST, and run until 2100 LMST.

Modelled and measured fluxes are displayed in Fig. 8. Net radiation has a significant positive bias (i.e. high MBE and RMSE); however, radiation tests in Sect. 3 show the radiation scheme to be accurate, and of higher accuracy than 2-D models for 3-D scenarios. Given the high roof plan fraction, the underprediction of roof surface temperature (and therefore of $L\uparrow$) is probably a large contributor. The parameterization of $L\downarrow$, the inaccurate specification of facet radiative and thermal parameters, and differing observation and model "source areas" probably also contribute to the disagreement.

There also appears to be poor agreement in terms of turbulent/storage ($Q_h/\Delta Q_s$) partitioning. However, output from the Town Energy Balance Model (TEB; Masson 2000) averaged over 7 days (August 12–18, 1992) all exhibiting meteorological conditions similar to August 15, i.e. clear with a strong sea breeze, demonstrates similar model–observation differences; that is, much smaller ΔQ_s and greater Q_h than observed (Masson et al. 2002). Masson et al. point out that advection below the measurement/forcing level appears in the ΔQ_s (residual) term in the observations, but in the Q_h term in offline model simulations forced by observations, such as the present TUF-3D simulations. Thus, the sea-breeze conditions and the proximity of the site to an upwind water body suggest that advection is probably a significant contributor to the model–observation discrepancy. Indeed, at the onset of the sea breeze (0800–0900 LMST) observed residual ΔQ_s increases dramatically, while it is the modelled Q_h that increases rapidly at this time (Fig. 8).

TUF-3D facet-average roof and street temperatures are compared with modelled (Masson et al. 2002) and measured (helicopter-mounted thermal scanner and truck-mounted IRT) temperatures in Fig. 9. In order to match the 'kinetic' surface temperatures (T_{sfc}) output by TEB, TUF-3D temperatures are also 'kinetic', i.e. they result
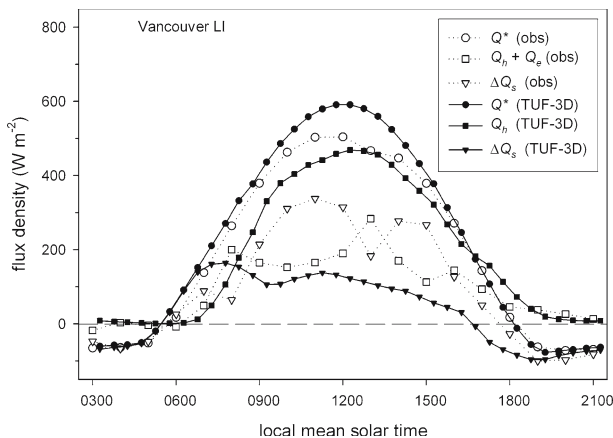
Fig. 8 Vancouver LI observed and TUF-3D energy balance components, August 15, 1992
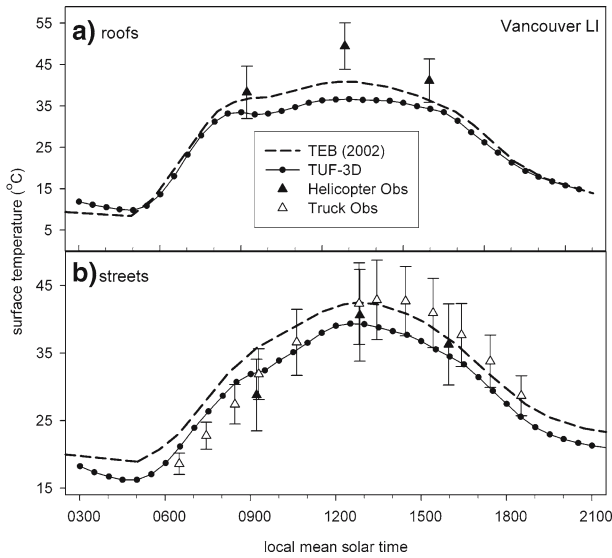
Fig. 9 Diurnal evolution of modelled and observed (helicopter-mounted thermal scanner and truck-mounted IRT) Vancouver LI roof and street surface kinetic temperatures on August 15, 1992. Helicopter observation error bars are GIS-derived standard deviations of pixel-resolution spatial variability from scanner data. Truck observation error bars are standard deviations of all observations from the traverse route. TEB results are extracted from Masson et al. (2002)

from solution of surface energy balances, while the observations are converted to kinetic temperatures assuming a surface emissivity of 0.95.

TUF-3D roof temperature evolution is similar to that modelled by TEB; both models significantly underestimate midday temperatures and clearly respond to the onset of the sea breeze in the morning (Fig. 9a). Model–observation disagreement probably results from uncertainty in parameter specification, notably uncertainty in the roof roughness length, insulation layer thickness, and radiative parameters, and the $z_{0m}/z_{0h} \leq 200$ limitation may also play a role (see Sect. 2.3.3). The discrepancy between the small source areas represented by the forcing data (which are measured very close to roof level) and the local scale roof temperatures sampled by the helicopter may also play a role. A simulation with reduced roughness length and doubled insulation thickness results in excellent agreement with the helicopter observations and reduces the positive $Q*$ bias reported earlier by nearly half (not shown).

TUF-3D street surface temperatures are slightly lower than the Masson et al. (2002) results (Fig. 9b), probably because the Lemonsu et al. (2004) canopy thermal production term (Sect. 2.3.3) is included in TUF-3D but not in the Masson et al. (2002) TEB version. Modelled temperatures are reasonable in terms of magnitude, but lack the observed lag in temperature evolution by about 1 h. This lag may be partially due to the truck-mounted IRT bias towards street centres, and therefore to sunlit portions of the street. The TUF-3D average patch temperature of the central third of the street displays some of the observed temporal shift, while small changes in street z_{0m} and k enable the model to completely reproduce the lag (not shown). Helicopter observations are of ground-surface temperature, not just streets, derived by masking roof areas on the thermal image using GIS data.

Individual facet-average wall temperatures are compared against truck-mounted IRT observations in Fig. 10. Overall, agreement is good, especially during periods when solar forcing is driving surface temperature: the south-facing (south) wall all day, the west wall in the afternoon, and the east wall during the morning. Shaded walls are too warm by 2–4°C. The TUF-3D canyon temperature is higher than that observed by truck-mounted thermometers (not shown), suggesting that insufficient canopy venting may play a role. But given the well-developed sea-breeze conditions, it is likely that advective cooling of the canopy air took place, but is not included in the model formulation. Shaded wall temperatures are significantly improved with increased canopy venting and wall roughness (not shown). The statistics bear out the above observations (Table 3), with the shaded north walls performing less well than the sunlit south walls. Low east wall r^2 is related to a lag in the modelled temperature evolution relative to the observations. Wall apparent temperature averaged over the four directions is in good agreement with observations (not shown). Most important in terms of thermal anisotropy at the neighbourhood and local scales are the inter-facet surface temperature differences. The model effectively reproduces the north–south and east–west wall differences in terms of timing (i.e. r^2 in Table 3) and slightly underestimates the peak magnitudes (not shown) due to overestimation of
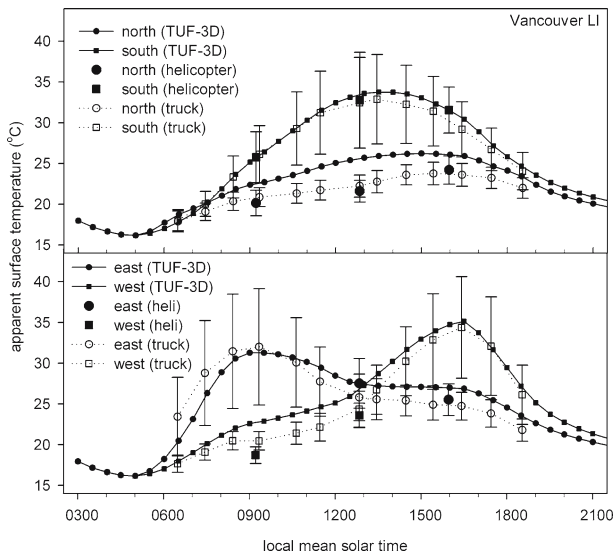
Fig. 10 Observed (truck and helicopter) and TUF-3D modelled facet-average apparent surface temperatures of north-, south-, east- and west-facing walls

Table 3 TUF-3D performance statistics for Vancouver LI facet-average apparent surface temperatures and apparent surface temperature differences (°C) as compared to 0630–1830 LMST *truck-mounted* IRT observations (13 observations). N = north, S = south, E = east, W = west

	Street	N wall	S wall	E wall	W wall	S − N	E − W	wall avg. − street
MBE	−0.7	2.1	0.5	0.5	1.4	−1.5	−0.8	1.8
RMSE	2.9	2.2	0.8	1.9	1.6	1.7	2.1	4.0
r^2	0.91	0.93	0.99	0.66	0.98	0.98	0.99	0.59

shaded wall temperatures. The wall-street temperature difference demonstrates less agreement for the same reason, and also as a result of the street temperature lag.

5.2 Basel Sperrstrasse (sub-facet comparison)

Detailed measurements of a west-south-west/east-north-east oriented canyon ($H/W =$ 1.24) in downtown Basel, Switzerland (47.57°N, 7.58°E) were conducted as part of the BUBBLE campaign (Rotach et al. 2005). The area is characterised by closely spaced buildings with mainly pitched roofs. In addition to tower mounted flux and meteorological observations, detailed within-canyon surface temperature measurements were conducted with an array of thermal IRTs and a thermal scanner, allowing for a model-observation comparison of surface temperatures at the sub-facet scale.

Parameters are fixed prior to simulation and are based on local geometrical indices and construction materials, and on tabulated thermal and radiative parameters (Table 2a, b). June 26, 2002 is chosen because it has mostly clear skies and lies within the BUBBLE IOP. Measurements at $z \approx 32$ m above the canyon floor provide the forcing data. TUF-2D simulations begin at 0000 LMST June 25 (to allow for model spin-up) and finish at 0000 LMST June 27; an identical simulation is run for July 8 (with July 7 as the spin-up day). Six 15° field of view (FOV) radiometers and two 60° FOV radiometers were deployed to measure surface temperatures within the canyon. IRT set-up details are given in the Appendix.

Figure 11 and Table 4 show the model-observation comparison. Agreement is good, particularly considering the large simplifications inherent in the model (e.g. no balconies, windows, cars, sloped roofs etc.) relative to the spatial scale of temperature measurement, and the uncertainties in choosing input parameters and matching the observed IRT FOVs with model patch ranges. The patterns of temperature evolution are well reproduced with the exception of midday overestimation at the north side of the street and a shift in the north-north-west (NNW) facing wall's afternoon peak. The former appears to result from an observed street surface temperature decrease between 0800 and 0900 LMST that is not well correlated with any measured meteorological variable (e.g. radiation, air temperature, wind speed), while the latter would be improved with specification of either a different canyon axis angle or greater wall thermal admittance. The statistics also indicate that the NNW-facing wall ($r^2 \approx 0.90$) and the north side of the street (RMSE = 4.0°C) are least well modelled (Table 4). Nevertheless, RMSE normalised by mean facet diurnal temperatures ranges remains below 16% for every facet. July 8 results are very similar to those just presented for June 26, with improved agreement on the timing of the NNW-facing wall's afternoon peak and on the street's north side temperature (not shown).

The temporal evolution of intra-facet temperature differences is reasonably well-reproduced (Fig. 12), again considering the small sizes of the areas sampled by the IRTs and the complexity of the surface structure and materials that are not included in the model. Magnitudes are at times slightly different, and visually diverge significantly only for the south-south-east (SSE)-facing wall, whose observed bottom-top temperature difference approximates zero during the morning hours when the model finds a significant positive difference due to the proximity of the bottom of the SSE-facing wall to the warm, sunlit (north) portion of the street. July 8 intra-facet temperature
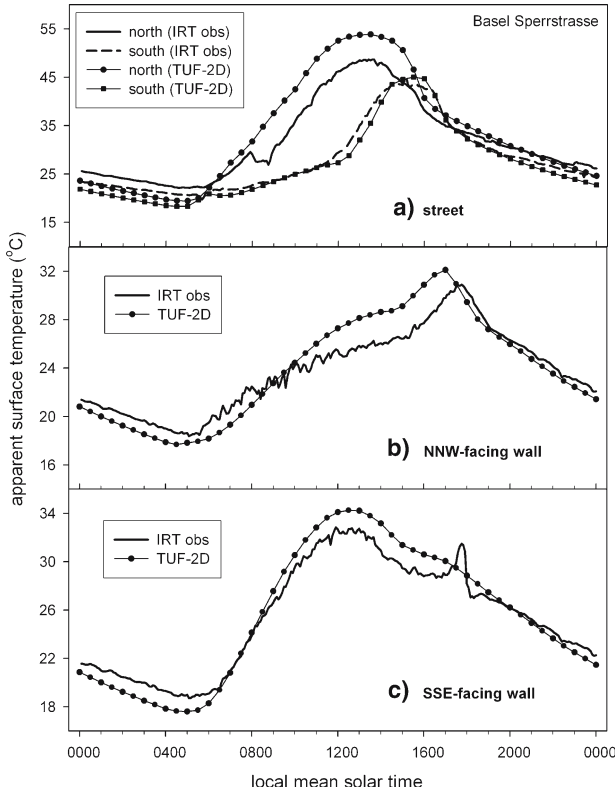
Fig. 11 Basel Sperrstrasse IRT temperatures (obs) plotted with corresponding TUF-2D apparent surface temperatures for June 26, 2002. NNW-facing and SSE-facing wall temperatures are facet 'averages' from 60° FOV IRTs

Table 4 TUF-2D performance statistics for Basel Sperrstrasse canyon apparent surface temperatures (°C) from 0000–2400 LMST June 26 (289 observations). S = south side, N = north side, SSE = south-south-east facing, NNW = north-north-west facing, top = top portion of wall, bottom = bottom portion of wall, all = wide range of wall sampled (FOV = 60°)

	Street (S)	Street (N)	SSE wall (top)	SSE wall (bottom)	SSE wall (all)	NNW wall (top)	NNW wall (bottom)	NNW wall (all)
MBE	−1.1	1.7	−0.3	0.3	0.2	−0.8	−0.6	0.2
RMSE	1.6	4.0	1.6	1.3	1.2	1.9	1.8	1.5
r^2	0.98	0.96	0.94	0.99	0.99	0.88	0.90	0.92

difference results are very similar to those just presented for June 26, and are therefore omitted for the sake of brevity.

6 Conclusions

A new sub-facet scale urban energy balance model, "Temperatures of Urban Facets in 3-D" (TUF-3D), is constructed to investigate urban surface temperature at several
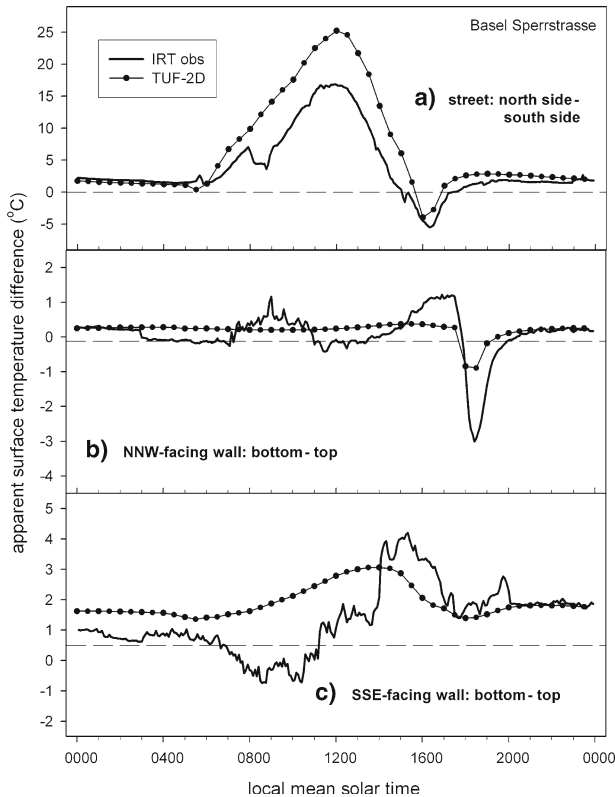
Fig. 12 Basel Sperrstrasse IRT observed and TUF-2D modelled apparent surface temperature *differences* for June 26, 2002

scales. TUF-3D is unique relative to other urban energy balance models in that it combines several attributes necessary to model the surface temperature distribution at sub-facet scales: 3-D geometry, rigorous treatment of radiation exchange at the sub-facet scale, and solution of the energy balance at the sub-facet scale. TUF-3D is therefore a useful tool relative to other urban energy balance models if (a) knowledge of the diurnal evolution of 3-D distributions of surface temperature and/or radiative exchanges at the sub-facet scale is important; or, (b) the goal is to investigate the impacts of the sub-facet scale variation of surface radiative and thermal properties, or the radiative impacts of sub-facet scale geometrical structures.

TUF-3D uses the radiosity approach based on inter-patch view factors and ray tracing to model radiative exchange between the identical square patches that compose the model. Conduction and surface temperature are treated similar to Arnfield (1990), while the convection scheme closely follows the approach taken in several 2-D canyon models (e.g. Masson 2000). Following tests of the model components, the full model is tested against observations from two cities during clear summer days, and shown to perform well overall in terms of both facet-average and sub-facet surface temperatures. These results point to a range of further tests to perform. Tests of the full model were limited to two days at two separate sites, and should be performed for

a greater range of urban sites, weather conditions and seasons to more successfully separate model weaknesses from incorrect parameter specification and/or processes influencing the observations that are beyond the range of the model's intent (e.g. sea breezes).

TUF-3D is primarily limited due to its simplicity. For example, it lacks a realistic vegetation sub-model and its geometry and its convection treatment are both relatively crude. Further model development should focus on the introduction of common urban features such as trees and peaked roofs, and the introduction of a sub-facet scale flow model. Nevertheless, the present version of TUF-3D is a first step towards overcoming limitations to the investigation of both surface temperature distributions and anisotropy in thermal remote sensing of urban areas. It simulates surface temperature in a mostly simulated environment (i.e. it requires only a few forcing inputs, which also have the potential to be modelled). The combination of TUF-3D with the SUM sensor-view model (Soux et al. 2004) will permit the investigation of the causes of both urban effective thermal anisotropy and spatial surface temperature variation, and of their sensitivities to a range of factors. Furthermore, the model has application in a number of other areas, including, for example, the investigation of 3-D radiative loads and exchanges at several spatio-temporal scales, and the impacts of sub-facet scale complexity on urban surface temperature.

Appendix: Basel Sperrstrasse IRT Observations

Six 15° FOV radiometers record the 'upper' and 'lower' apparent surface temperatures of both walls as well as of the north and south portions of the street (Fig. A1 and Table A1). A further two 60° FOV radiometers record 'average' wall surface temperatures of the two walls. Due to set-up constraints on IRT location and orientation angles, and to the spherical/elliptical nature of the IRT FOVs superimposed on the surfaces, the terms 'upper', 'lower', and 'average' are employed somewhat loosely. The precise sub-facet range within each sensor's field of view is estimated from BUBBLE field notes, and the corresponding sub-facet patch-average apparent temperatures are extracted from the modelled results (Fig. A1 and Table A1).
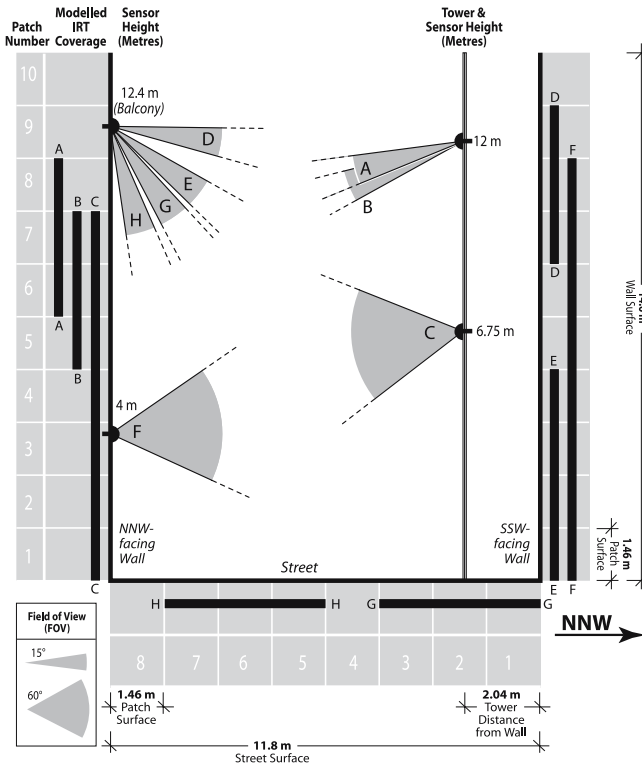
Fig. A1 Basel Sperrstrasse canyon IRT setup during the IOP and the corresponding model patch ranges employed in the observation-TUF-2D comparison. Capital letters (i.e. A, B,...H) differentiate IRTs and the corresponding TUF-2D patch ranges with which they are compared. IRTs with along-canyon orientation components are collapsed into the equivalent 2-D angle. Model patches are numbered (1–10 for walls, 1–8 for the street)

Table A1 IRT locations and view arrangements, and corresponding TUF-2D patch ranges

IRT	Wall viewed	IRT height a.g.l. (m)	Field of view (°)	Depression angle (°)	Along-canyon angle (°)	TUF-2D patch range[a]
A	NNW-facing ('top')	12.0	15	11	45	6–8
B	NNW-facing ('bottom')	12.0	15	16[c]	45	5–7
C	NNW-facing ('all')	6.8	60	8	0	1–7
D	SSE-facing ('top')	12.4	15	8	0	7–9
E	SSE-facing ('bottom')	12.4	15	37	0	1–4
F	SSE-facing ('all')	4.0[b]	60	−5	0	1–8
G	street ('north')	12.4	15	55	0	1–3
H	street ('south')	12.4	15	74	0	5–7

[a] See Fig. A1

[b] Estimate based on photo of instrument and surroundings

[c] Shifted during the observation period; likely larger for much of the IOP

References

Aida M (1982) Urban albedo as a function of the urban structure—a model experiment. Boundary-Layer Meteorol 23:405–413

Arnfield AJ (1988) Validation of an estimation model for urban surface albedo. Phys Geog 9:361–372

Arnfield AJ (1990) Canyon geometry, the urban fabric and nocturnal cooling: a simulation approach. Phys Geog 11:220–239

Arnfield AJ, Grimmond CSB (1998) An urban canyon energy budget model and its application to urban storage heat flux modeling. Energy Buildings 27:61–68

Arnfield AJ, Mills GM (1994) An analysis of the circulation characteristics and energy budget of a dry, asymmetric, east–west urban canyon II: energy budget. Int J Climatol 14:239–261

Ashdown I (1994) Radiosity: a programmer's perspective. John Wiley & Sons, New York, 496 pp

Ashie Y, Ca VT, Asaeda T (1999) Building canopy model for the analysis of urban climate. J Wind Eng and Ind Aerodyn 81:237–248

ASHRAE (1981) American society of heating, refrigerating and air conditioning engineers handbook 1982 applications. ASHRAE, Atlanta GA

Bruse M, Fleer H (1998) Simulating surface–plant–air interactions inside urban environments with a three-dimensional numerical model. Environ Model Software 13:373–384

Carlson TN, Dodd JK, Benjamin SG, Cooper JN (1981) Satellite estimation of the surface energy balance, moisture availability and thermal inertia. J Appl Meteorol 20:67–87

Christen A, Vogt R (2004) Energy and radiation balance of a central european city. Int J Climatol 24:1395–1421

Cionco RM (1965) A mathematical model for air flow in a vegetative canopy. J Appl Meteorol 4:517–522

Clarke JA (1985) Energy simulation in building design. Adam Hilger, Bristol, 400 pp

Coceal O, Belcher SE (2004) A canopy model of mean winds through urban areas. Quart J Roy Meteorol Soc 130:1349–1372

Cole RJ, Sturrock NS (1977) The convective heat exchange at the external surface of buildings. Building Environ 12:207–214

Groleau D, Fragnaud F, Rosant JM (2003) Simulation of the radiative behavior of an urban quarter of marseille with the SOLENE model. In: preprint, Fifth International Conference on Urban Climate, Lodz, Poland, Sept 1–5, 2003, International Association for Urban Climate, pp 335–338

Harman IN, Barlow JF, Belcher SE (2004) Scalar fluxes from urban street canyons. Part II: model. Boundary-Layer Meteorol 113:387–409

Hottel HC, Sarofim AF (1967) Radiation heat transfer. McGraw-Hill, New York, 520 pp

Iqbal M (1983) An introduction to solar radiation. Academic Press, Toronto, 390 pp

Jacobson MZ (1999) Fundamentals of atmospheric modeling. Cambridge University Press, 656 pp

Johnson GT, Oke TR, Lyons TJ, Steyn DG, Watson ID, Voogt JA (1991) Simulation of surface urban heat islands under 'ideal' conditions at night part 1: theory and tests against field data. Boundary-Layer Meteorol 56:275–294

Kanda M, Kawai T, Kanega M, Moriwaki R, Narita K, Hagishima A (2005a) A simple energy balance model for regular building arrays. Boundary-Layer Meteorol 116:423–443

Kanda M, Kawai T, Nakagawa K (2005b) A simple theoretical radiation scheme for regular building arrays. Boundary-Layer Meteorol 114:71–90

Kawai T, Kanda M (2003) Three dimensional radiation model for urban canopy. Ann J Hydro Eng 47:55–60 (in Japanese)

Kondo H, Kikegawa Y (2003) Temperature variation in the urban canopy with anthropogenic energy use. Pure Appl Geophys 160:317–324

Kusaka H, Kondo H, Kikegawa Y, Kimura F (2001) A simple single-layer urban canopy model for atmospheric models: comparison with multi-layer and slab models. Boundary-Layer Meteorol 101:329–358

Lemonsu A, Grimmond CSB, Masson V (2004) Modeling the surface energy balance of the core of an old mediterranean city: marseille. J Appl Meteorol 43:312–327

Louis JF (1979) A parametric model of vertical eddy fluxes in the atmosphere. Boundary-Layer Meteorol 17:187–202

Macdonald RW (2000) Modelling the mean velocity profile in the urban canopy layer. Boundary-Layer Meteorol 97:25–45

Macdonald RW, Griffiths RF, Hall DJ (1998) An improved method for estimation of surface roughness of obstacle arrays. Atmos Environ 32:1857–1864

Martilli A, Clappier A, Rotach MW (2002) An urban surface exchange parameterisation for mesoscale models. Boundary-Layer Meteorol 104:261–304

Mascart P, Noilhan J, Giordani H (1995) A modified parameterization of flux–profile relationships in the surface layer using different roughness length values for heat and momentum. Boundary-Layer Meteorol 72:331–344

Masson V (2000) A physically based scheme for the urban energy budget in atmospheric models. Boundary-Layer Meteorol 94:357–397

Masson V, Grimmond CSB, Oke TR (2002) Evaluation of the town energy balance (TEB) scheme with direct measurements from dry districts in two cities. J Appl Meteorol 41:1011–1026

Mills G (1993) Simulation of the energy budget of an urban canyon—I. Model structure and sensitivity test. Atmos Environ 27B:157–170

Mills G (1997a) An urban canopy-layer climate model. Theor Appl Climatol 57:229–244

Mills G (1997b) The radiative effects of building groups on single structures. Energy Buildings 25: 51–61

Nakamura Y, Oke TR (1988) Wind, temperature and stability conditions in an east–west oriented urban canyon. Atmos Environ 12:2691–2700

Nunez M, Oke TR (1977) The energy balance of an urban canyon. J Appl Meteorol 16:11–19

Oke TR (1987) Boundary layer climates. Routledge, London, 435 pp

Oke TR (1988) The urban energy balance. Prog Phys Geogr 12:471–508

Prata AJ (1996) A new long-wave formula for estimating downward clear-sky radiation at the surface. Quart J Roy Meteorol Soc 122:1127–1151

Raupach MR (1992) Drag and drag partition on rough surfaces. Boundary-Layer Meteorol 60:375–395

Rotach MW (1993) Turbulence close to a rough urban surface part I: Reynolds stress. Boundary-Layer Meteorol 65:1–28

Rotach MW (1995) Profiles of turbulence statistics in and above an urban street canyon. Atmos Environ 29:1473–1486

Rotach MW, Vogt R, Bernhofer C, Batchvarova E, Christen A, Clappier A, Feddersen B, Gryning S-E, Martucci G, Mayer H, Mitev V, Parlow E, Richner H, Roth M, Roulet Y-A, Ruffieux D, Salmond JA, Shatzmann M, Voogt JA (2005) BUBBLE—an urban boundary layer meteorology project. Theor Appl Climatol 81:231–261

Rowley FB, Algren AB, Blackshaw JL (1930a) Effects of air velocity on surface coefficients. Trans ASHRAE 36:123–136

Rowley FB, Algren AB, Blackshaw JL (1930b) Surface conductances as affected by air velocity, temperature, and character of surface. Trans ASHRAE 36:429–446

Rowley FB, Eckley WA (1932) Surface coefficients as affected by wind direction. Trans ASHRAE 38:33–46

Siegel R, Howell JR (2001) Thermal radiation heat transfer, 4th edn. Taylor and Francis-Hemisphere, Washington, 868 pp

Sievers U, Zdunkowski W (1985) A numerical simulation scheme for the albedo of city street canyons. Boundary-Layer Meteorol 33:245–257

Soux A, Voogt JA, Oke TR (2004) A model to calculate what a remote sensor 'sees' of an urban surface. Boundary-Layer Meteorol 112:109–132

Stull RB (2000) Meteorology for scientists and engineers, 2nd edn. Brooks/Cole, Pacific Grove, USA, 502 pp

Terjung WH, Louie SS-F (1974) A climatic model of urban energy budgets. Geogr Anal 6:341–367

Voogt JA, Grimmond CSB (2000) Modeling surface sensible heat flux using surface radiative temperatures in a simple urban area. J Appl Meteorol 39:1679–1699

Voogt JA, Oke TR (1997) Complete urban surface temperatures. J Appl Meteorol 36:1117–1132

Voogt JA, Oke TR (1998) Effects of urban surface geometry on remotely sensed surface temperature. Int J Remote Sens 19:895–920

Willmott CJ, Ackleson SG, Davis RE, Feddema JJ, Klink KM, Legates DR, O'Donnell J, Rowe CM (1985) Statistics for the evaluation and comparison of models. J Geophys Res C 90:8995–9005

Wu L (1995) An urban canopy layer surface energy balance climate model. Ph.D. Dissertation, University of California, Los Angeles